Gamma-Rhythmic Gain Modulation

Citation: Ni, Jianguang et al. "Gamma-Rhythmic Gain Modulation." Neuron 92, 1 (October 2016): 240–251 © 2016 Elsevier

As Published: http://dx.doi.org/10.1016/J.NEURON.2016.09.003

Publisher: Elsevier/Cell Press

Persistent URL: http://hdl.handle.net/1721.1/112247

Version: Final published version: final published article, as it appeared in a journal, conference proceedings, or other formally published context

Article

Neuron

Gamma-Rhythmic Gain Modulation

Highlights

- Visually induced gamma rhythmically modulates the gain of spike responses
- Visually induced gamma also rhythmically modulates behavioral reaction times (RTs)
- Gamma phases leading to strong spike responses and to short RTs are very similar
- Optogenetically induced gamma in higher visual area causes similar gain modulation

Authors

Jianguang Ni, Thomas Wunderle,
Christopher Murphy Lewis,
Robert Desimone, Ilka Diester,
Pascal Fries

Correspondence

pascal.fries@esi-frankfurt.de

In Brief

Ni et al. show that visually and optogenetically induced gamma rhythmically modulate the gain of spike responses to visual stimuli, and that this directly impacts behavioral reaction times. Thus, gamma-band coherence can modulate effective connectivity consistent with the communication-through-coherence hypothesis.

Ni et al., 2016, Neuron *92*, 240–251
October 5, 2016
http://dx.doi.org/10.1016/j.neuron.2016.09.003

Neuron
Article

Gamma-Rhythmic Gain Modulation

Jianguang Ni,[1,2] Thomas Wunderle,[1] Christopher Murphy Lewis,[1] Robert Desimone,[3] Ilka Diester,[1,5] and Pascal Fries[1,4,6,*]
[1]Ernst Strüngmann Institute (ESI) for Neuroscience in Cooperation with Max Planck Society, Deutschordenstraße 46, 60528 Frankfurt, Germany
[2]International Max Planck Research School for Neural Circuits, Max-von-Laue-Straße 4, 60438 Frankfurt, Germany
[3]Department of Brain and Cognitive Sciences, McGovern Institute for Brain Research, Massachusetts Institute of Technology, Cambridge, MA 02139, USA
[4]Donders Institute for Brain, Cognition, and Behaviour, Radboud University Nijmegen, Kapittelweg 29, 6525 EN Nijmegen, Netherlands
[5]Present address: Optophysiology, Bernstein Center and BrainLinks-BrainTools, University of Freiburg, Albertstraße 23, 79104 Freiburg, Germany
[6]Lead Contact
*Correspondence: pascal.fries@esi-frankfurt.de
http://dx.doi.org/10.1016/j.neuron.2016.09.003

SUMMARY

Cognition requires the dynamic modulation of effective connectivity, i.e., the modulation of the postsynaptic neuronal response to a given input. If postsynaptic neurons are rhythmically active, this might entail rhythmic gain modulation, such that inputs synchronized to phases of high gain benefit from enhanced effective connectivity. We show that visually induced gamma-band activity in awake macaque area V4 rhythmically modulates responses to unpredictable stimulus events. This modulation exceeded a simple additive superposition of a constant response onto ongoing gamma-rhythmic firing, demonstrating the modulation of multiplicative gain. Gamma phases leading to strongest neuronal responses also led to shortest behavioral reaction times, suggesting functional relevance of the effect. Furthermore, we find that constant optogenetic stimulation of anesthetized cat area 21a produces gamma-band activity entailing a similar gain modulation. As the gamma rhythm in area 21a did not spread backward to area 17, this suggests that postsynaptic gamma is sufficient for gain modulation.

INTRODUCTION

The flexible modulation of effective connectivity is central to many cognitive functions. Selective attention is a prime example, in which the responses to an attended stimulus are routed forward with enhanced effective connectivity (Reynolds et al., 1999). Enhanced effective connectivity corresponds to an enhanced gain, i.e., a stronger response to a constant stimulus. Two mechanisms for gain modulation might be provided by neuronal gamma-band synchronization. On the one hand, gamma-band synchronization among pre-synaptic neurons makes synaptic inputs arrive coincidently at postsynaptic neurons, which increases their postsynaptic impact (Azouz and Gray, 2003; Salinas and Sejnowski, 2001). On the other hand, gamma-band synchronization among postsynaptic neurons entails a characteristic sequence of network excitation followed by inhibition (Atallah and Scanziani, 2009; Buzsáki and Wang, 2012; Salkoff et al., 2015; Vinck et al., 2013), which likely modulates the response to synaptic input. Input that is consistently synchronized to gamma phases with high excitability might benefit from enhanced gain and thereby enhanced effective connectivity, a proposal referred to as the ‘‘communication-through-coherence’’ (CTC) hypothesis (Fries, 2005, 2015).

Gain increases for coincident synaptic inputs have been suggested by mathematical models (Salinas and Sejnowski, 2001). In vivo intracellular recordings from neurons in the visual cortex of anesthetized cats have demonstrated an adaptive coincidence detection mechanism (Azouz and Gray, 2003). Simultaneous recordings in anesthetized macaque V1 and V2 show that V2 spikes are preceded by coincident V1 spikes (Zandvakili and Kohn, 2015). V1 spike coincidence is provided by gamma-band synchronization, and indeed, V1 spikes occurring at the V1 gamma phase of strongest spiking are most often followed by V2 spikes (Jia et al., 2013). This mechanism likely enhances the impact of attended stimuli. V4 neurons driven by attended stimuli show enhanced gamma-band synchronization (Fries et al., 2001), whose strength predicts the attentional reaction-time benefit on a given trial (Womelsdorf et al., 2006).

Mathematical models have also supported the idea that gamma-band synchronization among postsynaptic neurons rhythmically modulates their gain, such that input consistently arriving at high-gain phases benefits from enhanced effective connectivity (Börgers and Kopell, 2008). Simultaneous recordings at multiple sites within or across visual areas of awake cats and macaques demonstrate that effective connectivity, indexed by power covariation, is systematically modulated by the phase relation between respective local gamma rhythms (Womelsdorf et al., 2007). Similarly, in anesthetized macaque V1, directed influences between recording sites are modulated by the respective gamma phase relation (Besserve et al., 2015).

The gain enhancement through synchronization between pre- and postsynaptic neurons might subserve the selective routing of attended stimuli. Neurons in macaque V4 are selectively entrained by the gamma rhythm of V1 inputs representing the attended stimulus (Bosman et al., 2012; Grothe et al., 2012). For this selective entrainment to cause enhanced effective

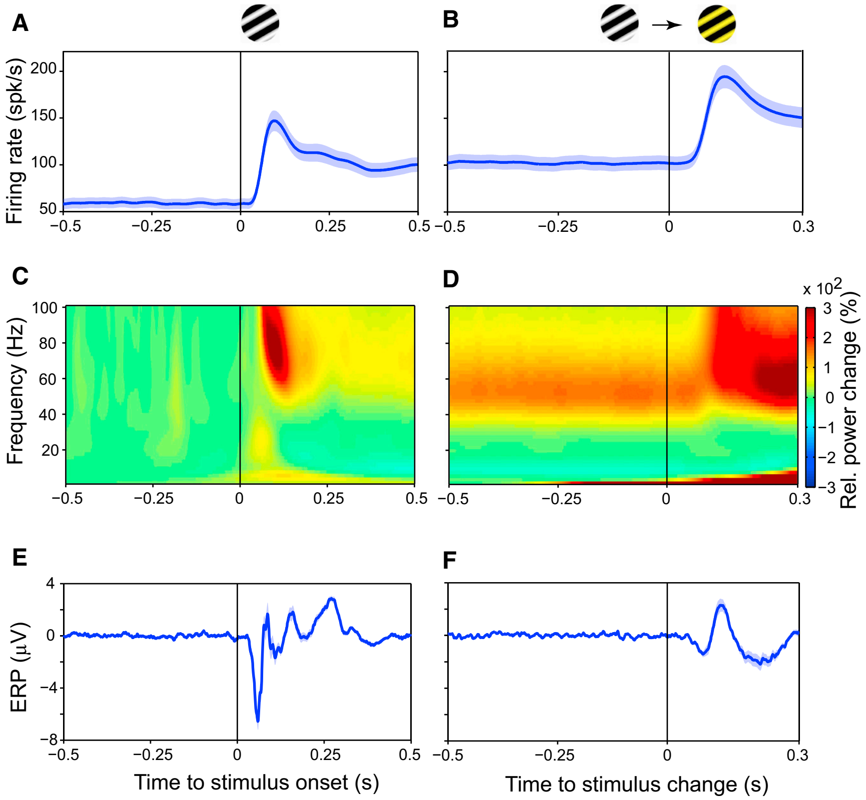

Figure 1. Visually Induced MUA Responses, LFP Power, and Event-Related Potentials in Awake Macaque V4

(A and B) MUA firing rate, smoothed with a Gaussian kernel (SD = 12.5 ms, truncated at ±2 SD).

(C and D) Percentage LFP power change relative to the pre-stimulus baseline period from 0.5 s to 0.25 s before stimulus onset.

(E and F) Event-related potentials, i.e., time-domain averages of the LFP across trials.

(A, C, and E) Temporal modulation around stimulus onset.

(B, D, and F) Temporal modulation around stimulus color change.

(A–F) All images show grand averages over all 94 recording sites in both monkeys.

(A, B, E, and F) Shaded regions around the lines indicate ±1 SEM across recording sites. See also Figure S1.

connectivity, the V4 gamma has to modulate gain rhythmically, as a function of gamma phase. This has been a core requirement of the CTC hypothesis (Fries, 2015), but experimental evidence has so far been lacking. The definitive test for gain modulation by postsynaptic gamma phase uses externally timed test inputs placed at different gamma phases. Such test inputs have been used in two seminal studies that probed consequences of optogenetic pulse trains driving fast-spiking interneurons in mouse somatosensory cortex. When the local neuronal population was entrained by a 40 Hz pulse train, its response to a stimulation of a vibrissa was modulated by the 40 Hz phase at which the stimulus was delivered (Cardin et al., 2009). This rhythmic modulation of neuronal responses also impacts behavior, as shown in a subsequent study that used the same approach in barrel cortex of mice performing a tactile detection task. Detection of low-salience stimuli was improved when input to the optogenetically entrained cortex coincided with high-excitability phases (Siegle et al., 2014).

If visually induced gamma in V4 exerted similar gain modulation effects on externally timed test inputs, the abovementioned selective inter-areal gamma-band synchronization for attended stimuli might indeed implement enhanced effective connectivity during visual attention. Here, we present evidence from two experiments, one combining electrophysiology with behavioral analysis in awake macaque visual cortex and a second combining electrophysiology with optogenetic stimulation in anesthetized cat visual cortex. In macaques, we recorded multi-unit activity (MUA) and local field potentials (LFP) in area V4, while a visual stimulus induced a sustained gamma rhythm. At a random time, we changed stimulus color, which gave a change-related firing rate response. We found that the magnitude of this response depended on the V4 gamma phase at which the change-related input to V4 occurred. The gamma-phase dependent response modulation went substantially beyond an additive superposition of a constant response on ongoing gamma-modulated firing, demonstrating the modulation of multiplicative gain. The same gamma phase that led to maximal firing rate responses also led to shortest behavioral reaction times, suggesting that the effect has direct functional relevance. As visual stimulation induces partly synchronized gamma-band activity across ventral visual areas (Bastos et al., 2015a; Bosman et al., 2012; Grothe et al., 2012; Jia et al., 2013; Roberts et al., 2013), this effect could emerge at any stage. To test whether gamma in a higher visual area was sufficient to generate the effect, we used optogenetics in anesthetized cats. Constant optogenetic stimulation of area 21a, the cat homolog of macaque V4 (Payne, 1993), induced sustained gamma-band activity in area 21a, that did not spread to area 17, the homolog of V1. When a visual stimulus was presented at random gamma phases, the phase, at which the change-related input to area 21a occurred, modulated the stimulus response, suggesting that an isolated postsynaptic gamma rhythm is sufficient to generate a multiplicative gain modulation.

RESULTS

Visually Induced Gamma Rhythm Modulates Gain

MUA and LFP were recorded from three to four electrodes simultaneously in area V4 of two macaques performing an attention task. Visual stimulation with a patch of grating in the receptive fields (RFs) of the recorded neurons induced clear enhancements of V4 MUA rate (Figures 1A and 1B) and LFP gamma power (Figures 1C and 1D). Figure S1 shows examples of visually

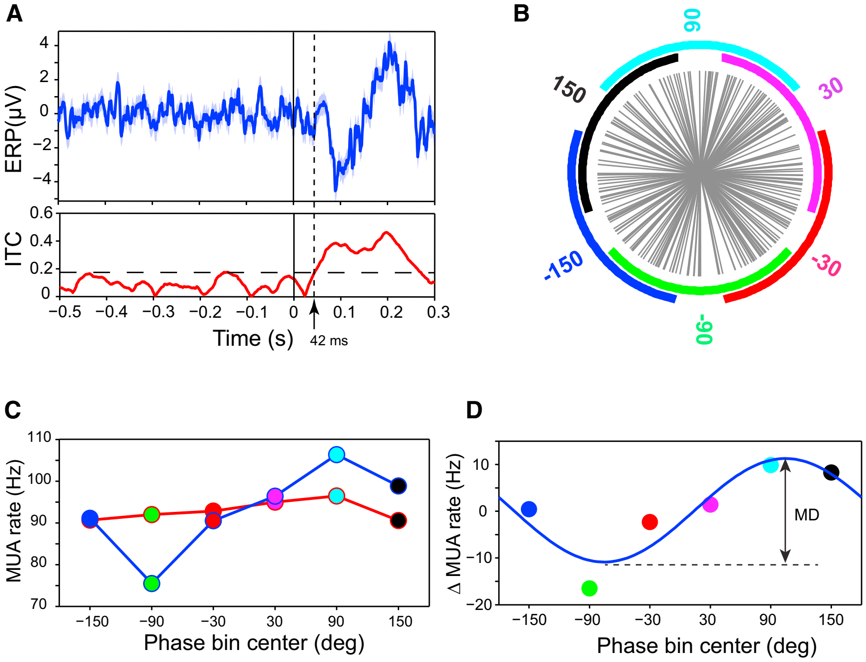

Figure 2. Example Analysis of Response Modulation by Pre-input Phase in Awake Macaque V4

(A) The top panel shows the ERP that was evoked in an example recording site by stimulus changes. The shaded region around the line indicates ± 1 SEM across trials. The bottom panel shows the corresponding ITC at 10 Hz, together with the significance threshold, indicating the first change-evoked response at 42 ms after stimulus change.

(B) Each gray spoke represents the pre-input LFP phase for the gamma band (50 Hz) in one trial (see Experimental Procedures for details of phase estimation). The trials were grouped into six phase bins. For each phase bin, the 75 trials with phases closest to the phase-bin center were chosen for further processing.

(C) Blue line: MUA response as a function of pre-input gamma phase. After phase binning, both the gamma phases and the corresponding MUA responses were averaged over the trials assigned to the respective phase bin. Red line: same as the blue line, but showing the additive MUA response component.

(D) Colored dots: multiplicative MUA response component, obtained by subtracting the additive MUA response component from the (total) MUA response. The smooth blue curve represents a cosine fit. The cosine modulation depth (MD) is quantified as indicated.

induced gamma-band oscillations. Stimulus onset evoked a transient, time-locked LFP component visible in the time-domain LFP average, the event-related potential (ERP) (Figure 1E). At a random time between 0.5 s and 5 s after stimulus onset, the grating in the RFs changed from black/white to black/yellow (Figures 1B, 1D, and 1F). We analyzed the trials in which the stimulus in the RFs was behaviorally relevant and in which the monkey responded correctly, i.e., in which the stimulus change in the RFs triggered a behavioral response. We found that the stimulus change induced a substantial firing rate response (Figure 1B). Preceding the stimulus change, the visually induced gamma-band response was sustained (Figure 1D). At the same time, the ERP was flat (Figure 1F), indicating that gamma oscillations were not aligned to the upcoming stimulus change, because stimulus changes occurred at random times between 0.5 s and 5 s after stimulus onset.

This allowed us to analyze the ongoing LFP phase before the stimulus change and test whether it predicts the MUA response to the stimulus change. Figure 2 illustrates this for an example recording site. We first estimated the time of arrival of the stimulus-change-induced synaptic inputs by calculating the inter-trial coherence (ITC) of the LFP (Figure 2A, see Experimental Procedures). ITC quantifies the phase locking of the LFP across trials, which sensitively captures both phase-locked LFP amplitude changes and phase resets. As the ERP after stimulus change was dominated by a theta-alpha band component (Figure 1F), we used the ITC at the 10 Hz bin, which covers the 5–15 Hz range. For the example site, the 10 Hz ITC was enhanced at 42 ms after stimulus change, which we defined as "input time". The median (±SEM) input times for the two monkeys were 41 ± 2 ms (monkey P) and 43 ± 4 ms (monkey R). We defined the LFP phase estimated for the last sample before the input time as the pre-input phase.

Pre-input phase distributions were expectedly random, and we binned phases into six bins as indicated by the colored sectors in Figure 2B for the gamma-phase distribution. MUA responses to the stimulus change were quantified for the time, when the trial-averaged MUA peaked, which we call the "peak time". For the example MUA, the peak time was at 134 ms after stimulus change. MUA responses depended systematically on pre-input gamma phase (blue line in Figure 2C). A cosine fitted to the observed MUA responses had a significantly greater amplitude than shuffle controls ($p = 0.025$, non-parametric randomization test based on random pairing of pre-input phases and post-input MUA responses).

The dependence of the MUA response on pre-input gamma phase might be due to a simple additive superposition of a constant MUA response onto ongoing gamma-modulated MUA firing; note that MUA is typically synchronized to the visually induced LFP gamma rhythm (Fries et al., 2008). If the MUA response peak would coincide with a peak of gamma-modulated MUA firing, the response would be enhanced, and vice versa. The size of such an additive superposition effect can be estimated by mathematically adding the average MUA response to the pre-input MUA record after phase binning (van Elswijk et al., 2010). Specifically, we defined a surrogate input time at 150 ms before the actual input time. We analyzed the LFP phase at the surrogate input time, binned trials according to those phases, and calculated per phase bin the average MUA record between the surrogate and the actual input time. Onto those

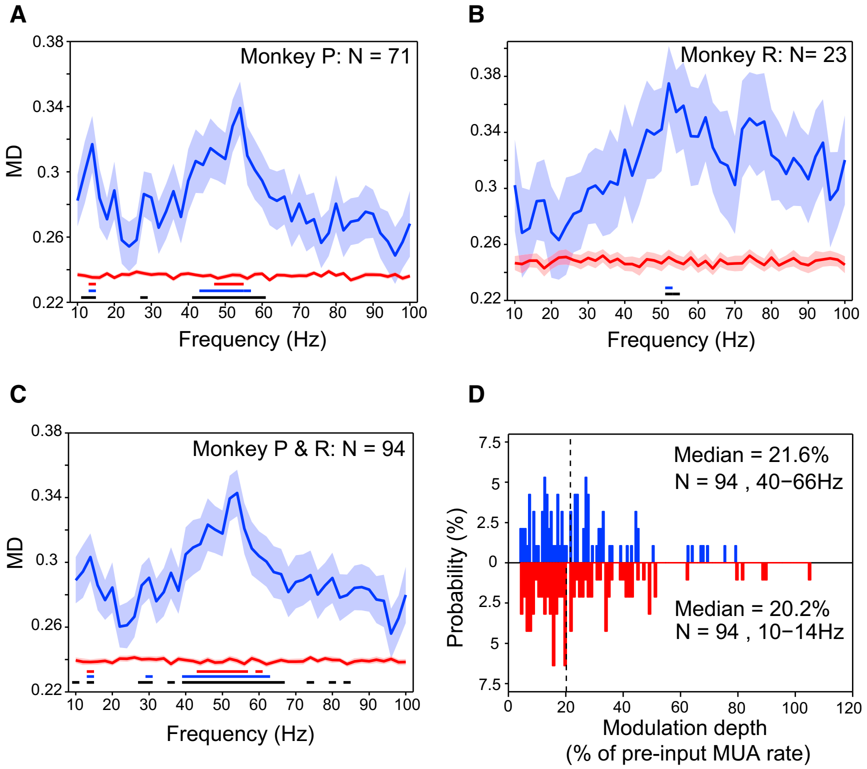

Figure 3. Gain Modulation Is Prominent for the Gamma Rhythm in Awake Macaque V4

(A) Blue curve: modulation depth of the multiplicative MUA response component as a function of the frequency, for which the pre-input phase was determined. The average over all 71 sites of monkey P after z-transformation per site (see Experimental Procedures) is shown (red curve: bias estimate). The shaded regions indicate ±1 SEM across recording sites. The horizontal lines at the bottom of the plot indicate significance levels after correction for multiple comparisons across frequencies: black lines for $p < 0.05$; blue lines for $p < 0.01$; and red lines for $p < 0.001$.

(B) Same format as (A), averaged over all 23 sites of monkey R.

(C) Same format as (A), averaged over all 94 sites of both monkeys combined.

(D) Histogram of modulation depths of the multiplicative MUA response component, expressed as percentage of pre-input MUA rate. The blue histogram on top shows values obtained with binning according to pre-input phase in the gamma-frequency range found significant in (C), i.e., 40–66 Hz; the red histogram on the bottom shows values obtained with binning according to pre-input phase in the alpha-beta-frequency range found significant in (C), i.e., 10–14 Hz. The dashed vertical lines indicate median values.

bin-wise surrogate MUA records, we mathematically added the MUA response to the stimulus change, averaged across all trials, but now aligned to the surrogate input time. The resulting additive MUA response component as function of gamma phase is shown as the red line in Figure 2C. The additive MUA response component was subtracted from the (total) MUA response to obtain the multiplicative MUA response component (Figure 2D). Phase-dependent modulation depth (MD) of the multiplicative MUA response component was quantified by a cosine fit (smooth curve in Figure 2D) and exceeded shuffle controls ($p = 0.03$, same test as for Figure 2C).

The analysis illustrated in Figure 2 for an example MUA recording site was performed for all 94 MUA recording sites of both macaques; in addition, a bias estimate for the cosine fit was obtained for all sites as explained in Experimental Procedures. The observed modulation depths consistently exceeded the bias estimates in the gamma band and also in a band that overlaps with both the classical alpha and beta bands, and which we therefore address as alpha-beta band (Figures 3A–3C). To quantify effect size, we expressed the modulation depths as percent of the pre-input MUA rate (Figure 3D). Effect sizes had median values of 20.2% for the alpha-beta band (10–14 Hz) and 21.6% for the gamma band (40–66 Hz) and showed distributions including values exceeding 50% (see Experimental Procedures for quantification of effect sizes).

Gamma Phase Modulates Behavioral Reaction Time

We hypothesized that the phase of visually induced gamma also modulates behavioral reaction times (RTs) in response to the stimulus change. To investigate this, we proceeded similarly to the analysis of MUA responses (see Experimental Procedures). Trials were binned according to pre-input LFP phase, and for each phase bin, RTs were averaged. Indeed, RTs were modulated by the phase of pre-input LFP oscillations in the gamma band (Figure 4A). A non-parametric permutation test with correction for multiple comparisons across frequencies revealed significance for the frequency bins centered at 48–52 Hz, which reflect spectral energy between 42 and 58.5 Hz. The phase of this LFP gamma component modulated RT by a median of 13 ms (Figure 4B). Thus, the pre-input gamma phase has a direct influence on behavior.

So far, we have shown (1) that pre-input gamma phase partly predicts the MUA response to stimulus change and (2) that pre-input gamma phase partly predicts behavioral RTs. Therefore, we next investigated whether pre-input gamma phases leading to short RTs are similar to those leading to strong MUA responses. We first selected the MUA recording sites, which showed an individually significant response modulation by pre-input gamma phase (N = 69). For those sites, we determined the pre-input gamma phase leading to maximal MUA responses and the pre-input gamma phase leading to shortest RTs (both were determined from the respective cosine function fits). To quantify the similarity between those phases, we took the cosine of the phase difference, which gives a value of 1 for equal phases and a value of -1 for opposite phases. The average cosine spectrum (Figure 4C) shows values close to 1 in the gamma range. In the 48–52 Hz range, for which pre-input phase was significantly predictive of behavioral RT, phase differences were significantly non-uniformly distributed ($p = 0.03$, V-test; Berens, 2009) with a mean phase difference of merely 15.3 degrees. Thus, pre-input gamma phases leading to short RTs also lead to strong MUA responses. This suggests that the influence of gamma phase on MUA responses has functional relevance.

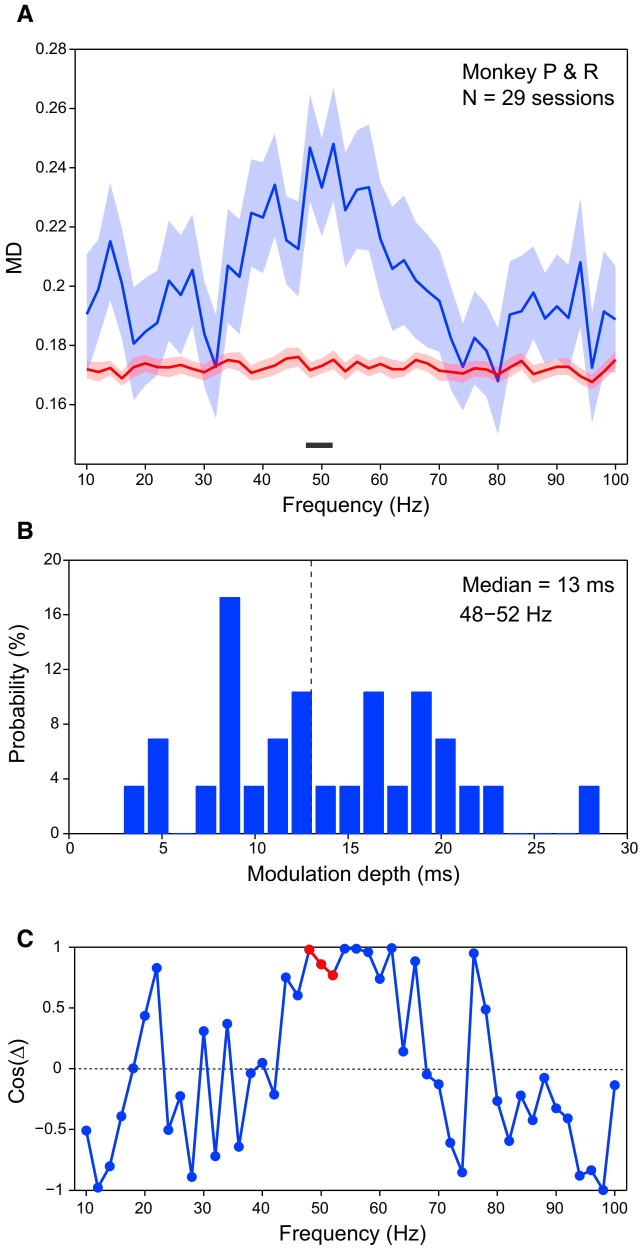

Figure 4. In Awake Macaque V4, Gamma Phase Modulates Reaction Time, and Similar Gamma Phases Lead to Short Behavioral Reaction Times and Strong Neuronal Responses

(A) Blue: modulation depth of behavioral RTs by pre-input phase (after z-transformation of RTs per session, by subtraction of mean and division by SD across trials in a session) (red: bias estimate). The shaded regions indicate ±1 SEM across sessions. The black horizontal bar on the bottom indicates significant modulation in the gamma band from 48 to 52 Hz ($p < 0.05$, non-parametric permutation test, corrected for multiple comparisons across frequencies).

(B) Distribution of the modulation depths of RTs by pre-input 48–52 Hz phase.

(C) The cosine of the difference (Δ) between phases leading to shortest RTs and phases leading to strongest neuronal responses. Cosine values close to one indicate that phases leading to short RTs are close to phases leading to strong neuronal responses. For the frequency range of 48–52 Hz (red dots), phase differences are significantly non-uniform ($p = 0.03$), with an average phase difference of merely 15.3 degrees.

(A–C) All plots combine the data of both monkeys ($n = 29$ sessions).

Effects of the Phase of Isolated, Optogenetically Induced Gamma

We showed that the phase of ongoing, visually induced gamma in area V4 modulates both the MUA response to a stimulus change and the corresponding behavioral reaction time. Yet, it remains unclear whether this effect emerged in V4 or at earlier processing stages. When the visual stimulus induced a gamma rhythm in V4, it most likely also induced gamma rhythms in earlier visual cortical areas, which were partly coherent with the V4 gamma. Several previous studies demonstrated visually induced gamma-band coherence between V1 and V4 (Bosman et al., 2012; Brunet et al., 2014; Grothe et al., 2012), and further studies established that gamma in lower visual areas entrains gamma in higher visual areas in a feedforward manner (Bastos et al., 2015a, 2015b; Bosman et al., 2012; Jia et al., 2013; Michalareas et al., 2016; Roberts et al., 2013; van Kerkoerle et al., 2014). Thus, the effect of V4 gamma phase might emerge at earlier stages. This would be fully in line with our general hypothesis, that a local gamma rhythm modulates the response to randomly timed synaptic test inputs (see Discussion). Nevertheless, we sought to test whether an isolated gamma rhythm could have the same effect. We found that this test could be elegantly performed, when using gamma induced by constant light stimulation of neurons expressing Channelrhodopsin (ChR2). Several previous reports have shown that local ChR2-expressing neuronal populations generate clear gamma rhythms in response to light that is constant or smoothly ramping up (Adesnik and Scanziani, 2010; Akam et al., 2012; Lu et al., 2015). That is, while the light did not contain any temporal structure in the gamma-frequency range, the gamma rhythm was generated by the neuronal network, most likely through reverberant interactions between excitatory and inhibitory neurons (Tiesinga and Sejnowski, 2009; Whittington et al., 2000).

For these experiments, we used the anesthetized cat as a model system (N = 2 animals). We injected recombinant adeno-associated viral vectors to express ChR2 in cortical neurons [AAV9-CamKIIα-hChR2(H134R)-eYFP]. Vectors were injected into area 21a, the cat homolog of macaque area V4 (Figure 5A) (Payne, 1993). After 4 to 6 weeks of expression, recordings were performed under general anesthesia. Subsequently, the animal was perfused and the brain processed histologically. Confocal microscopy showed ChR2-eYFP expression in cortical neurons (Figure 5B). Area 21a recordings showed clear responses to the local application of blue light (473 nm) (Figure 5C). Constant light for a period of 1.25 s induced a pronounced gamma-band rhythm (Figures 5C, middle panel and 6). Figure S2 shows examples of gamma-band oscillations induced by constant optogenetic stimulation. Simultaneous recordings

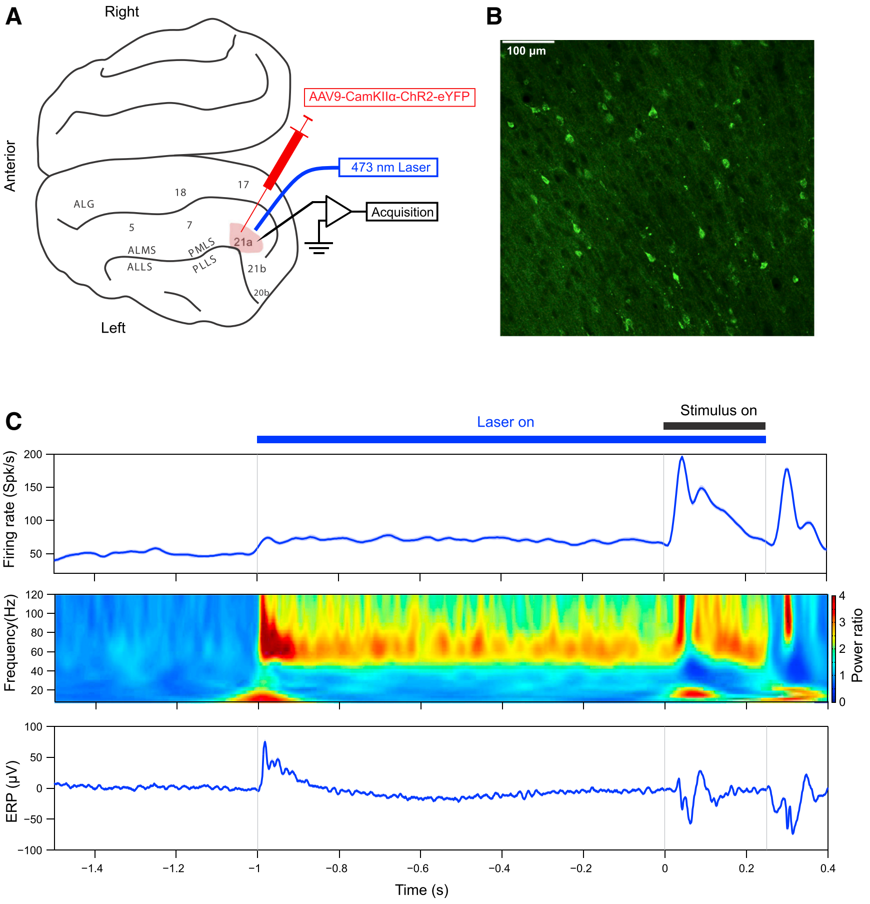

Figure 5. Viral Injection and Expression; Optogenetically and Visually Induced MUA Responses, LFP Power and Event-Related Potentials in Anesthetized Cat Area 21a

(A) In an initial surgery, the viral vector AAV9-CamKIIα-hChR2(H134R)-eYFP was injected into cat area 21a. After 4 to 6 weeks of expression, 473 nm laser light was applied through a fiber placed above area 21a, visual stimuli were shown, and electrophysiological recordings performed from area 21a.

(B) Example histological section, showing the distribution of eYFP-labeled neurons in area 21a through fluorescence microscopy.

(C) Responses of one example recording site during optogenetic and visual stimulation as indicated by the horizontal lines above the top panel. Laser stimulation commenced first, followed 1 s later by visual stimulation. Top: MUA firing rate. Middle: LFP power. Bottom: Event-related potential. The shaded regions around the lines in the top and bottom panels indicate ±1 SEM across trials; they are hardly visible behind the actual lines. See also Figure S2.

in area 17, the cat homolog of macaque area V1 and the source of major input to area 21a, suggested that optogenetically induced gamma in area 21a did not propagate in the feedback direction to area 17 (Figure 6). The absence of feedback propagation of gamma might be partly due to the general anesthesia; yet, it is consistent with recent reports of a feedforward nature of gamma in the awake state (Bastos et al., 2015a; Michalareas et al., 2016; van Kerkoerle et al., 2014). In any case, it provided the conditions for the intended test.

Having established this optogenetically induced gamma in area 21a, we produced synaptic test inputs through visual stimulation. Visual stimuli were presented at 1 s after onset of optogenetic stimulation and lasted for 0.25 s. We analyzed the MUA response to visual stimulus onset as a function of the LFP phase prior to the input time. We used the same approach as in the analysis of the macaque V4 data, with two differences: (1) Because the visual stimulus onset evoked an ERP with substantial gamma-band components (Figure 5C), input time was based on the ITC at the 50 Hz bin, which covers the 25–75 Hz range. The resulting mean input times were 27.7 ± 0.3 ms (Cat 1) and 32.3 ± 0.9 ms (Cat 2). (2) Whereas the visually induced gamma peak frequencies in the two macaques happened to be almost identical, the optogenetically induced gamma peak frequencies differed across cats and recording sessions (Figures S3A and S3B). These differences were probably due to differences in local density of opsin expression, effective light intensity, the state of the anesthetized cat, or combinations of those factors. Therefore, we determined the optogenetically induced gamma peak frequency per recording site and aligned the analysis to it. We found that gamma induced locally in area 21a by optogenetic stimulation was sufficient to multiplicatively modulate the MUA response to visual stimulus onset (Figures 7A–7C). The median effect size was 21.8% (Figure 7D).

DISCUSSION

We found that gamma-band activity rhythmically modulates multiplicative gain. Gain modulation exceeded 50% in some cases and had a median size of slightly more than 20%. The findings held across gamma induced in awake macaque V4 by sustained visual stimulation and gamma induced in anesthetized cat area 21a by constant optogenetic stimulation. The awake macaque data allowed us to investigate the relevance of gamma phase for behavior. This showed that gamma phases leading to short behavioral reaction times were similar to gamma phases leading to strong MUA responses. Optogenetic stimulation allowed us to investigate the effect of “isolated” gamma in a higher visual area, that was most likely not preceded by substantial gamma in lower visual areas. This showed that such isolated optogenetically induced gamma leads to multiplicative gain modulation of similar size as visually induced gamma.

MUA responses in macaque V4 showed multiplicative gain modulation also for the alpha-beta phase. Alpha-beta oscillations are typically much larger than gamma oscillations, and it has been argued that therefore alpha, but not gamma, is suited to support CTC (Ray and Maunsell, 2015). However, we show

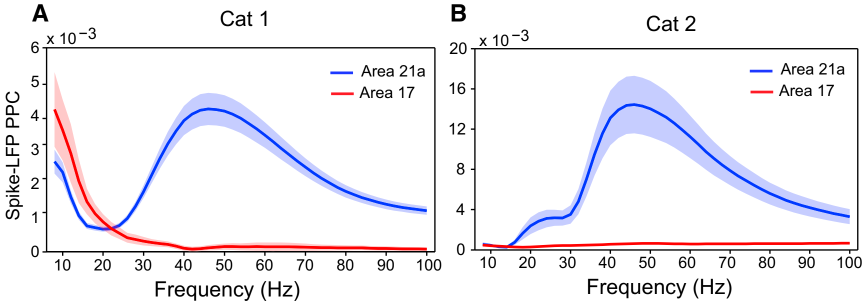

Figure 6. Optogenetic Stimulation of Area 21a Induces Gamma in Area 21a and Not in Area 17 in the Anesthetized Cat

(A) Spike-LFP locking in area 21a (blue) and area 17 (red) during optogenetic stimulation of area 21a in the absence of visual stimulation. Each line shows the average over all respective recording sites of cat 1 (area 21a: n = 57 and area 17: n = 11). The shaded regions indicate ±1 SEM across recording sites.

(B) Same as (A), but showing the averages over all respective recording sites of cat 2 (area 21a: n = 33 and area 17: n = 38).

that median gain modulation is 20.2% for alpha-beta and 21.6% for gamma. Criticism of the CTC hypothesis has also been based on stimulus-dependent gamma frequencies in V1 and on a short autocorrelation length of gamma (Ray and Maunsell, 2015). Yet, CTC depends neither on particular gamma frequencies nor on stable gamma frequencies, but on gamma coherence. Inter-areal gamma coherence is maintained for dynamically varying gamma frequencies (Lowet et al., 2016; Roberts et al., 2013) and can thereby turn the observed phase-dependent gain into coherence-dependent effective connectivity.

In a previous paper, we provided first evidence that effective connectivity between two visually driven local neuronal groups in awake cat or monkey visual cortex depends on the phase relation between the respective local gamma rhythms (Womelsdorf et al., 2007). For each pair of recording sites, we segmented the data into 0.25 s long epochs, estimated the phases of local neuronal rhythms, and sorted epochs into six bins, according to their phase relations. Per frequency, for which the phase relation was estimated, we quantified effective connectivity as the correlation between the respective power values across the epochs of a given phase-relation bin. We found that effective connectivity depended systematically on the phase relation, primarily in the gamma-frequency band. A subsequent mathematical modeling study simulated two gamma-synchronized neuronal groups and found that the gamma phase relation between the groups does not only determine their power correlation, but also their mutual transfer entropy (Buehlmann and Deco, 2010). Transfer entropy is an information theoretical measure that quantifies the statistical dependence between systems and is able to distinguish between driving and responding elements and therefore between shared and transmitted information. A recent experimental study investigated transfer entropy between multiple simultaneous recordings in anesthetized macaque area V1 (Besserve et al., 2015). Transfer entropy was influenced by the phase relation between local gamma-band rhythms. In particular, dynamic changes in the stimulus led to directed gamma-band waves and a relative increase in the amount of information flowing along the instantaneous direction of the gamma wave.

While these studies together strongly suggest that the phase relation among gamma-band rhythms affects the strength and direction of influences between the respective neuronal groups, the possibility remains that those phase relations are not the cause, but the consequence of the neuronal influences. It is conceivable that other mechanisms modulate effective connectivity, and that enhanced effective connectivity subsequently leads to particular phase relations. The current results provide compelling evidence that the gamma rhythm is actually a cause of modulations in effective connectivity. We show that the gain is modulated within each gamma cycle, as a function of gamma phase. If this gamma-rhythmic gain modulation were due to a mechanism other than the gamma rhythm itself, this mechanism would necessarily oscillate at the relatively high gamma frequency and in synchrony with the gamma rhythm (without actually being the gamma rhythm). While such arbitrarily complex assumptions can explain essentially any set of results, it is much more parsimonious and physiologically plausible that the gamma rhythm itself modulates gain rhythmically and thereby enhances the effective connectivity of inputs synchronized to gamma phases of high gain.

Our central experimental approach has been to assess the response to a temporally unpredictable visual event, i.e., a stimulus change in the monkey recordings and a stimulus onset in the cat recordings. Because the stimulus event is physically identical in all trials, the strength of the resulting synaptic input should be constant, at least at the earliest stages of visual processing (with the exception of uncontrolled fluctuations arising from physiological noise). Our finding that physically identical stimulus events lead to varying postsynaptic responses that depend systematically on the pre-input gamma phase unequivocally demonstrates the rhythmic modulation of postsynaptic gain. Importantly, we cannot conclude from our measurements that the postsynaptic gain modulation emerged in the very neurons from which we recorded the spiking activity. In the awake macaque experiments, the postsynaptic gain modulation might have emerged in any neuron on the way from the retina to the recorded V4 neurons. Yet, wherever the modulation emerged, it there constituted a postsynaptic modulation, because of our use of identical stimulus events across trials. Note that any modulation that emerged at an earlier stage would become visible in our analysis only if the gamma phase at this earlier stage were coherent with the gamma phase recorded in V4. Gamma coherence between early and intermediate level visual areas is clearly present, but of small magnitude (Bastos et al., 2015a; Bosman et al., 2012; Grothe et al., 2012), and typically not transitive across multiple processing stages (Zandvakili and Kohn, 2015). Thus, the gain modulation that we observed as a function of V4 gamma phase likely emerges fully or largely in V4. This interpretation is consistent with the results of the optogenetics experiments. Optogenetic stimulation induced a gamma rhythm in

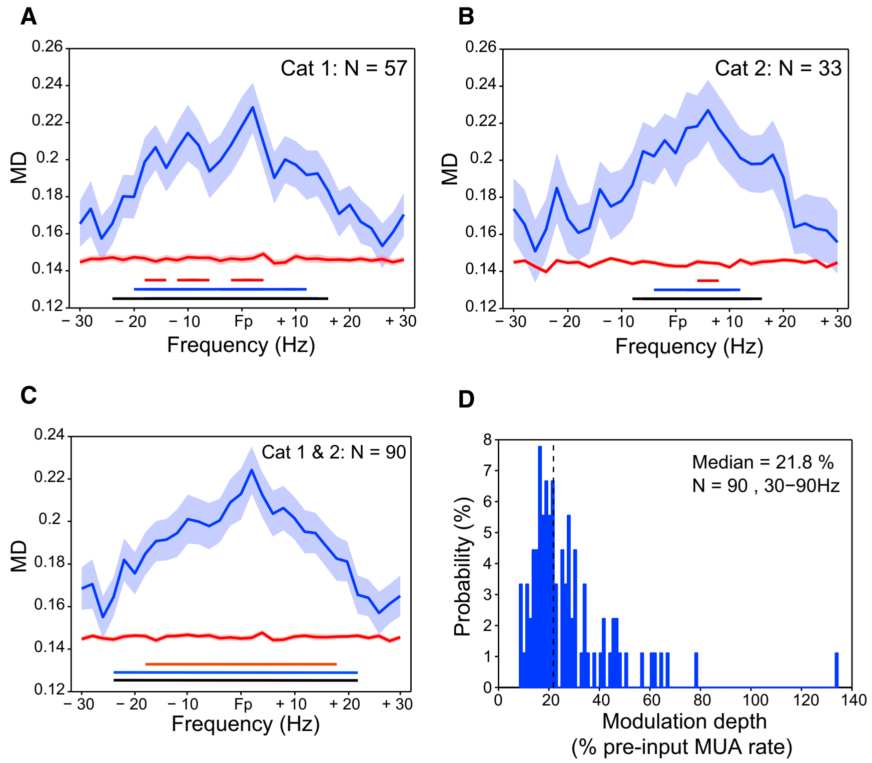

Figure 7. Gain Modulation by Optogenetically Induced Gamma in the Anesthetized Cat

(A) Blue curve: modulation depth of the multiplicative MUA response component as a function of the frequency, for which the pre-input phase was determined. The average over all 57 recording sites in area 21a of cat 1 after z-transformation per site (see Experimental Procedures) is shown. Per recording site, the spectral analysis was aligned to the gamma peak frequency (Fp) induced at that site by optogenetic stimulation (see Figure S3). The x axis shows frequencies relative to Fp (red curve: bias estimate). The shaded regions indicate ±1 SEM across recording sites. The horizontal lines at the bottom of the plot indicate significance level after correction for multiple comparisons across frequencies: black lines for $p < 0.05$; blue lines for $p < 0.01$; and red lines for $p < 0.001$.

(B) Same format as (A), averaged over all 33 area 21a sites of cat 2.

(C) Same format as (A), averaged over all 90 area 21a sites of both cats combined.

(D) Histogram of modulation depths of the multiplicative MUA response component, expressed as percentage of pre-input MUA rate. The dashed vertical line shows median. See also Figure S3.

area 21a and no appreciable gamma rhythm in area 17. The modulation of gain by the area 21a gamma phase was similar to the modulation found in the awake macaque. We note that it is not possible to fully equate strength and extent of optogenetically and visually induced gamma.

While visually and optogenetically induced gamma rhythms led to gain modulation of similar size, the actual physiologically relevant gain modulation likely exceeds our estimates for several reasons: (1) The barrages of synaptic input generated by the stimulus events might have created a partial ceiling effect. Gain modulation might be larger for individual synaptic inputs. (2) Noise in the electrophysiological assessment of the relevant gamma phase likely reduced the observed modulation depths. We estimated gamma phase from the LFP, which includes influences from functionally separate neurons and also measurement noise. Still, the LFP is a good approximation of the relevant membrane potential fluctuations (Haider et al., 2016). (3) Noise in the estimation of the pre-input gamma phase. Generally, frequency-specific phase estimation requires a finite-length time window. Therefore, the phase estimated for the pre-input time actually reflects the preceding epoch and, due to gamma's short autocorrelation length, this only approximates the phase at the pre-input time point. (4) The synaptic test inputs likely arrived not at one time point, but with a certain temporal distribution. This distribution must have been short relative to the gamma cycle, because otherwise any gain modulation effect would have been averaged out across gamma phases. Yet, some temporal spread was likely present, such that the true effect size is likely even larger than the observed one.

The likely temporal spread of stimulus-event-related synaptic inputs also precluded a simple interpretation of the absolute gamma phase leading to the maximal peak response. We determined this phase relative to the pre-input time, which we conservatively defined as the last time bin before LFP ITC deviated significantly from pre-stimulus-event values. While this approach safely excludes post-input data from the estimation of the pre-input phase, it introduces a certain delay between the estimated pre-input time and the actual temporal distribution of synaptic test inputs. This delay likely differed slightly across the different MUA clusters, e.g., due to uncertainty in ITC onset estimation and to actual physiological differences in the temporal spread of synaptic inputs. Even a delay of merely 5 ms will result in a phase rotation at 50 Hz of 90 degrees. Therefore, in order to interpret the phases leading to maximal peak responses, we compared them to the phases leading to shortest behavioral reaction times. Despite the substantial noise and uncertainty involved on both sides, this analysis revealed that, across different MUA recordings sites, gamma phases leading to shortest behavioral reaction times were close to gamma phases leading to strongest MUA responses. This suggests that the observed gamma phases leading to maximal responses are actually meaningful and that the gain modulation by the gamma rhythm has direct behavioral relevance.

EXPERIMENTAL PROCEDURES

Experiments were performed on two awake macaque monkeys and on two anesthetized cats. Data analysis for the two data sets followed the same approach.

Experiments on Macaques

Experiments were performed on two adult macaque monkeys, following the guidelines of the NIH and with approval by the National Institute of Mental Health Intramural Animal Care and Use Committee. Recordings were performed in area V4, while animals were awake and performing a selective visual attention task. The data analyzed here have been used in previous studies (Bosman et al., 2009; Brunet et al., 2014; Buffalo et al., 2010, 2011; Fries et al., 2001, 2008; Liang et al., 2005; Maris et al., 2013; Vinck et al., 2013; Womelsdorf et al., 2006, 2007).

Visual Stimulation and Behavioral Task

Visual stimulation, receptive field mapping, and attentional task are described in detail in Fries et al. (2008), and we report here only the essential points. Stimuli were presented on a 17 inch cathode ray tube monitor 0.57 m from the monkey's eyes with a refresh rate of 120 Hz non-interlaced. Stimulus generation and behavioral control were accomplished with the CORTEX software package (http://www.nimh.nih.gov/labs-at-nimh/research-areas/clinics-and-labs/ln/shn/index.shtml). The orientation of the drifting grating placed inside the receptive fields was selected so that it maximally coactivated the simultaneously recorded units. A second grating patch, rotated by 90 degrees and otherwise identical, was placed outside the receptive fields.

Several slightly different trial structures were used with different attentional cueing regimes (trial-by-trial cueing using as cue either short lines or the fixation point color, or trial-block cueing). As the attentional cueing regime is not relevant for the present analysis, we describe here the general trial structure. A trial started when the monkey touched a bar and directed its gaze within 0.7 degree of the fixation spot. After a baseline period of at least 1.5 s, the stimuli were presented, one cued as target and the other as distracter. Either the target or the distracter (equal probability) changed color (from black/white to black/yellow) at an unpredictable moment between 0.5 s and 5 s after stimulus onset (flat random distribution of change times across trials). If the distracter changed first, the target changed later, between the distracter change time and 5 s post stimulus onset. If the monkey released the bar within 0.15–0.65 s of a target change, a fluid reward was given. If the monkey released within the same time period after a distracter, a timeout was given. Trials were aborted if the monkey broke fixation or released the bar prematurely. In a typical recording session, monkeys completed 200 to 600 correctly performed trials.

Neurophysiological Recordings in Macaques

MRI was used to localize the prelunate gyrus. Recording chambers were implanted over the prelunate gyrus under surgical anesthesia. In each recording session, three to four tungsten microelectrodes (impedances around 1 MΩ at 1 kHz) were advanced separately through the intact dura at a very slow rate (1.5 μm/s) to minimize deformation of the cortical surface by the electrode ("dimpling"). Electrodes were horizontally separated by 650 or 900 μm. Standard electrophysiological techniques (Plexon MAP System) were used to obtain MUA and LFP recordings. For MUA recordings, the signals were filtered with a passband of 100 to 8,000 Hz, and a threshold was set interactively to retain the spike times of small clusters of units. For LFP recordings, the signals were filtered with a passband of 0.7 to 170 Hz and digitized at 1 kHz.

Experiments on Cats

Two adult female domestic cats were used. All procedures complied with the German law for the protection of animals and were approved by the regional authority (Regierungspräsidium Darmstadt). After an initial surgery for the injection of viral vectors and a 4–6 week period for virus expression, recordings were obtained during a terminal experiment under general anesthesia.

Viral Vector Injection

For the injection surgery, anesthesia was induced by intramuscular injection of Ketamine (10 mg/kg) and Medetomidine (0.02 mg/kg), cats were intubated, and anesthesia was maintained with N_2O:O_2 (60%/40%), Isoflurane (~1.5%) and Remifentanil (0.3 μg/kg/min). A rectangular craniotomy was made over the left hemisphere (AP: 0 to −8 mm and ML: 9 to 15 mm), area 21a was identified by the pattern of sulci and gyri, and the dura was removed over part of area 21a. Four injection sites in area 21a were chosen, avoiding major blood vessels, with horizontal distances between injection sites of at least 1 mm. At each site, a Hamilton Syringe (34G needle size; World Precision Instruments) was inserted under visual inspection to a cortical depth of 1 mm below the pia mater. Subsequently, 2 μL of viral vector solution (AAV9-CamKIIα-hChR2(H134R)-eYFP; titer 1.06 × 10^{13} GC/mL; Penn Vector Core) was injected at a rate of 150 nL/min. After each injection, the needle was left in place for 10 min before withdrawal to avoid reflux. Upon completion of injections, the dura opening was covered with silicone foil and a thin layer of silicone gel, the trepanation was filled with dental acrylic, and the scalp was sutured.

Neurophysiological Recordings in Cats

For the recording experiment, anesthesia was induced and initially maintained as during the injection surgery, only replacing intubation with tracheotomy and Remifentanil with Sufentanil. After surgery, during recordings, Isoflurane concentration was lowered to 0.6%–1.0%, eyelid closure reflex was tested to verify narcosis, and Vecuronium (0.25 mg/kg/h intravenous) was added for paralysis. Throughout surgery and recordings, Ringer's solution plus 10% glucose were given (20 mL/hr during surgery; 7 mL/hr during recordings) and vital parameters were monitored (electrocardiography, body temperature, and expiratory gases).

Each recording experiment consisted of multiple sessions. For each session, we inserted either single or multiple tungsten microelectrodes (~1 MΩ at 1 kHz, FHC), or three to four 32-contact probes (100 μm inter-site spacing, ~1 MΩ at 1 kHz; NeuroNexus or ATLAS Neuroengineering) in area 21a. In some sessions, an additional 3–4 of the same 32-channel probes were inserted into area 17. Standard electrophysiological techniques (Tucker-Davis Technologies system) were used to obtain MUA and LFP recordings. For MUA recordings, the signals were filtered with a passband of 700 to 7,000 Hz, and a threshold was set interactively to retain the spike times of small clusters of units. For LFP recordings, the signals were filtered with a passband of 0.7 to 250 Hz and digitized at 1,017 Hz.

Optogenetic stimulation was done with a 473 nm (blue) laser or with a 470 nm (blue) LED (Omicron). A 594 nm (yellow) laser was used as control and did not induce gamma-band activity (Figures S3C and S3D). Laser light was delivered to cortex through a 200 μm diameter multimode fiber, LED light through a 2 mm diameter multimode fiber. Fiber endings were placed just next to the recording sites with a slight angle relative to the electrodes. Illumination was applied to the recorded patch of area 21a for 1.25 s at a constant level. Intensity was titrated to induce clear gamma-band activity and totaled 1–10 mW when measured at the fiber ending. At 1 s after illumination onset, a visual stimulus was presented on a liquid crystal display (LCD, Samsung 2233RZ) with a screen update frequency of 120 Hz. Contact lenses were placed into the two eyes to equate their refraction as well as possible. The eye-to-screen distance was determined by the mean refraction index of the two eyes with their respective contact lenses. If necessary, prisms were used to align the eyes. Visual stimuli were presented for 0.25 s. They were either a static bar or a static grating patch inside the RFs of the recorded neurons or a static full-field grating. Stimulus generation and control used Psychtoolbox-3, a toolbox in MATLAB (MathWorks) (Brainard, 1997).

Histology

After the experiment, cats were euthanized with pentobarbital sodium and transcardially perfused with PBS followed by 4% paraformaldehyde. The brain was removed, postfixed in 4% paraformaldehyde, and subsequently soaked in 10%, 20%, and 30% sucrose-PBS solution, respectively, until the tissue sank. The cortex was sectioned in 50 μm thick slices. The slices were investigated with a confocal laser microscope (Nikon Instruments) for eYFP-labeled neurons.

Data Analysis

Spike Densities, Power Spectra, ERPs, and Spike-LFP Pairwise Phase Consistencies

MUA was smoothed with a Gaussian kernel (SD = 12.5 ms, truncated at ±2 SD) to obtain the spike density.

The LFP power spectra shown in Figures 1 and 5 were calculated with windows that were adjusted for each frequency to have a length of four cycles. Those windows were moved across the data in steps of 1 ms. For each frequency and window position, the data were Hann tapered, Fourier transformed, squared, and divided by the window length to obtain power density per frequency. These power values were then expressed as percent change of the average power in the baseline, −0.5 s to −0.25 s before onset of the visual stimulus in the macaque recordings and before onset of optogenetic stimulation in the cat recordings. Finally, power-change values were averaged over all recording sites.

ERPs were calculated as time-domain LFP averages after baseline subtraction.

Spike-LFP locking was quantified by calculating the spike-LFP pairwise phase consistency (PPC), a metric that is not biased by trial number, spike count, or spike rate (Vinck et al., 2010). Spike and LFP recordings were always taken from different electrodes. For each spike, the surrounding LFP in a window of ±2 cycles per frequency was Hann tapered and Fourier transformed. Per spike and frequency, this gave the spike-LFP phase, which should be similar across spikes, if they are locked to the LFP. This phase similarity is quantified by the PPC as the average phase difference across all possible pairs of spikes. If pairs of spikes from the same trial are excluded, this avoids effects of spike train history, like bursts, a procedure also followed here (Vinck et al., 2012). For a given MUA channel, spike-LFP PPC was calculated relative to all LFPs from different electrodes and then averaged.

Input Time and Pre-input LFP Phase

We investigated whether the LFP phase just before the time of synaptic test inputs (driven by stimulus change in the macaque and by stimulus onset in the cat) predicts the later MUA response. To estimate the time of synaptic inputs, the input time, we used the LFP, because it reflects the bulk synaptic inputs to the local neuronal group. We reasoned that the first significant stimulus-related response in the LFP should occur shortly after synaptic input arrives and it might partly reflect the synaptic input directly. As a particularly sensitive metric of LFP response onset, we calculated the ITC. The LFP was convolved with complex Morlet wavelets, defined as

$$w(t,f_o)=A\cdot\exp\left(-t^2/2\sigma_t^2\right)\cdot\exp(2\pi i f_o t),$$

with the normalization factor $A=\left(\sigma_t\sqrt{\pi}\right)^{-1/2}$, with t being the time, f_o the center frequency of the wavelet, and σ_t the SD of the Gaussian taper. We used wavelets with $\sigma_t=1/(\pi f_o)$, truncated at $\pm 3\sigma_t$, i.e., wavelets that are broad in the frequency domain and short in the time domain. The wavelet transform provided signal amplitude and phase per time and frequency. When phases are represented as unit-length complex vectors, the ITC is defined as the vector average across trials. ITC ranges from zero, indicating random phases, to one, indicating identical phases across trials. The ITC is defined per frequency. In the macaque data, the ERP to stimulus changes was dominated by a theta-alpha component (Figure 1F), and we therefore defined input time based on the ITC in the 10 Hz bin, which covers the 5–15 Hz range. In the cat data, the ERP to visual stimulus onsets reliably contained gamma-band components (Figure 5C), and we therefore defined input time based on the ITC in the 50 Hz bin, which covers the 25–75 Hz range. We defined the input time as the first time point for which the ITC values were significantly enhanced (non-parametric randomization test with multiple comparison correction across time). The convolution with wavelets was symmetric, such that it did not induce phase delays. As the ERPs occurred after the stimulus event, the wavelet transform, with its inherent temporal smoothing, most likely led to an underestimation of input times, which is the conservative approach in this case.

We needed to estimate the LFP phase as close as possible to the input time, while excluding any influence from after the input time. We created a bank of second-order band-pass Butterworth filters, with passband frequencies spaced between 10 and 100 Hz in steps of 2 Hz. Passband width scaled with passband frequencies, such that the lower (upper) cutoff was always at the passband frequency (F) minus (plus) F/8 Hz. The LFP starting from 0.4 s before the input time was filtered with this filter bank. Filtering was performed only in the forward direction to avoid any backward, i.e., non-causal, influence of the response to the test input on the estimation of the phase before the input. Subsequently, LFPs were downsampled to 250 Hz. Per LFP signal and per filter frequency, an autoregressive (AR) model of order 6 was fitted separately to each trial and then averaged over trials. The AR model was used to extrapolate the signal four cycles beyond the input time, which was done to avoid edge artifacts of the subsequent Hilbert transform (Chen et al., 2013). The Hilbert transform provided the analytic signal, from which the phase at the last sample before the input time was obtained, which we defined as the pre-input phase.

Responses to Stimulus-Driven Input and their Modulation by Pre-input Phase

We investigated the effect of the pre-input phase on the MUA response to stimulus events, i.e., stimulus changes in macaque V4 and stimulus onsets in cat area 21a. Per recording site, peri-event MUA spike densities were averaged over all trials, and a Gaussian function was fitted, whose mean was used as MUA peak response time for that recording site. Per trial, spike densities from 5 ms before to 5 ms after the MUA peak response time were averaged to obtain the MUA response.

Per recording site and per frequency, trials were grouped according to the pre-input phase into six phase bins centered at plus and minus 30, 90, and 150 degrees, respectively (see Figure 2B for illustration). For each phase bin, a number of trials with phases closest to the phase-bin center were chosen, and MUA responses were averaged over those trials. In macaques, this number was 75 trials, and in cats it was 200 trials.

A dependence of the MUA response on pre-input gamma phase might be due to a simple additive superposition of a constant MUA response onto the ongoing gamma-modulated MUA firing. Therefore, as explained in the main text, we obtained, per recording site, frequency, and phase bin, an estimated additive MUA response component. We subtracted the additive MUA response component from the (total) MUA response (of that recording site, frequency, and phase bin) to quantify the respective multiplicative MUA response component. To combine multiplicative MUA response components across recording sites, a z-transformation was done per recording site, by subtracting the mean and dividing by the SD of the total MUA response across trials.

The phase-dependent modulation of the z-transformed multiplicative MUA response components was quantified by fitting one cycle of a cosine function and defining the peak-to-peak amplitude as modulation depth (MD) (Figure 2D). We fitted both the cosine amplitude and phase to avoid strong assumptions about the phase leading to the strongest response. Because cosine fits without pre-determined phase always result in positive modulation depth, we estimated this bias. We randomly combined phases with z-transformed multiplicative MUA components and repeated the cosine fit 100 times. The average MD across those 100 randomizations is the bias estimate and is shown in Figures 3 and 7 as the red line.

To quantify the size of the phase-dependent modulation of the (non z-transformed) multiplicative MUA response component, i.e., to quantify effect size (Figures 3D and 7D), we used the modulation depths without subtraction of the bias (note: the bias from cosine fitting was not subtracted, but the additive MUA response component was subtracted). The bias is due to the fact that even noisy, i.e., random, variations in the multiplicative MUA response component will lead to a non-zero amplitude of the fitted cosine function. Importantly, those noisy variations are expected to randomly increase or decrease the multiplicative MUA response component, i.e., they are not expected to add to the true multiplicative MUA response component in a way that would systematically change the observed multiplicative MUA response component. This might appear counterintuitive given that we had to statistically test the observed multiplicative MUA response component against the bias estimate. To illustrate the situation, we would like to draw the analogy to extracellular spike recordings in the presence of the typical high-frequency noise. Spikes of a given neuron become visible when their amplitude exceeds the noise level. Yet, quantification of the peak-to-peak amplitude of the average spike waveform does not subtract the noise, because the noise superimposes with the spike randomly in a positive and negative manner and does not systematically change spike amplitude.

For the macaque data, we also analyzed behavioral RTs as a function of the pre-input phase. For this analysis, all available LFP channels were averaged, and trials were binned according to pre-input phase of the average LFP. For each phase bin, 75 trials with phases closest to the phase-bin center were chosen, and RTs of those trials were averaged. To combine phase-dependent RTs across sessions and subjects, a z-transformation was done per session, by subtracting the mean and dividing by the SD of the RTs of that session. Modulation depth was quantified as peak-to-peak amplitude of fitted cosine functions, for both the z-transformed data (Figure 4A) and the non-transformed data (Figure 4B).

Statistical Testing

Per recording site and per frequency, we obtained the observed MD and the corresponding bias estimate, i.e., per site, we obtained an MD spectrum and a bias spectrum. We tested whether those spectra differed consistently across recording sites. We calculated paired t tests between MD and bias spectra across sites. Statistical inference was not based directly on the t tests (and therefore corresponding assumptions will not limit our inference), but merely the resulting t-values were used as difference metric for the subsequent non-parametric permutation test. For each of 10,000 permutations, we did the following: we made a random decision per site to either exchange the MD spectrum and the bias spectrum or not; we performed the t test; we placed the largest t-value across all frequencies into the randomization distribution; this latter step implements multiple comparison correction across frequencies (Nichols and Holmes, 2002). Finally, we compared the observed t-values with the randomization distributions to derive p values for a two-sided test, corrected for the multiple comparisons across frequencies. All analyses were done with MATLAB and the FieldTrip toolbox (Oostenveld et al., 2011).

SUPPLEMENTAL INFORMATION

Supplemental Information includes three figures and can be found with this article online at http://dx.doi.org/10.1016/j.neuron.2016.09.003.

AUTHOR CONTRIBUTIONS

Conceptualization, J.N. and P.F.; Methodology, J.N., T.W., C.M.L., I.D., and P.F.; Software, J.N., T.W., and C.M.L.; Formal Analysis, J.N.; Investigation, J.N., T.W., C.M.L., and P.F.; Writing - Original Draft, J.N. and P.F.; Writing - Review & Editing, J.N., T.W., C.M.L., R.D., I.D., and P.F.; Supervision, I.D., R.D., and P.F.; and Funding Acquisition, I.D., R.D., and P.F.

ACKNOWLEDGMENTS

The authors thank Jarrod Dowdall, Dmitriy Lisitsyn, and Craig Richter for helpful suggestions on phase estimation using AR models; Alina Peter, Georgios Spyropoulos, and Martin Vinck for helpful suggestions on data analysis; and Iris Grothe and Wolf Singer for helpful suggestions on the text. P.F. acknowledges grant support by DFG (SPP 1665, FOR 1847, and FR2557/5-1-CORNET), EU (HEALTH-F2-2008-200728-BrainSynch, FP7-604102-HBP, and FP7-600730-Magnetrodes), a European Young Investigator Award, NIH (1U54MH091657-WU-Minn-Consortium-HCP), and LOEWE (NeFF). I.D. acknowledges grant support by DFG (SPP 1665), EU (ERC Starting Grant OptoMotorPath), BMBF (Bernstein Award 2012), LOEWE (NeFF), and the Minna-James-Heinemann Foundation.

Received: June 23, 2016
Revised: August 16, 2016
Accepted: August 24, 2016
Published: September 22, 2016

REFERENCES

Adesnik, H., and Scanziani, M. (2010). Lateral competition for cortical space by layer-specific horizontal circuits. Nature *464*, 1155–1160.

Akam, T., Oren, I., Mantoan, L., Ferenczi, E., and Kullmann, D.M. (2012). Oscillatory dynamics in the hippocampus support dentate gyrus-CA3 coupling. Nat. Neurosci. *15*, 763–768.

Atallah, B.V., and Scanziani, M. (2009). Instantaneous modulation of gamma oscillation frequency by balancing excitation with inhibition. Neuron *62*, 566–577.

Azouz, R., and Gray, C.M. (2003). Adaptive coincidence detection and dynamic gain control in visual cortical neurons in vivo. Neuron *37*, 513–523.

Bastos, A.M., Vezoli, J., Bosman, C.A., Schoffelen, J.M., Oostenveld, R., Dowdall, J.R., De Weerd, P., Kennedy, H., and Fries, P. (2015a). Visual areas exert feedforward and feedback influences through distinct frequency channels. Neuron *85*, 390–401.

Bastos, A.M., Vezoli, J., and Fries, P. (2015b). Communication through coherence with inter-areal delays. Curr. Opin. Neurobiol. *31*, 173–180.

Berens, P. (2009). CircStat: A MATLAB toolbox for circular statistics. J. Stat. Softw. *31*, 1–21.

Besserve, M., Lowe, S.C., Logothetis, N.K., Schölkopf, B., and Panzeri, S. (2015). Shifts of gamma phase across primary visual cortical sites reflect dynamic stimulus-modulated information transfer. PLoS Biol. *13*, e1002257.

Börgers, C., and Kopell, N.J. (2008). Gamma oscillations and stimulus selection. Neural Comput. *20*, 383–414.

Bosman, C.A., Womelsdorf, T., Desimone, R., and Fries, P. (2009). A microsaccadic rhythm modulates gamma-band synchronization and behavior. J. Neurosci. *29*, 9471–9480.

Bosman, C.A., Schoffelen, J.M., Brunet, N., Oostenveld, R., Bastos, A.M., Womelsdorf, T., Rubehn, B., Stieglitz, T., De Weerd, P., and Fries, P. (2012). Attentional stimulus selection through selective synchronization between monkey visual areas. Neuron *75*, 875–888.

Brainard, D.H. (1997). The psychophysics toolbox. Spat. Vis. *10*, 433–436.

Brunet, N.M., Bosman, C.A., Vinck, M., Roberts, M., Oostenveld, R., Desimone, R., De Weerd, P., and Fries, P. (2014). Stimulus repetition modulates gamma-band synchronization in primate visual cortex. Proc. Natl. Acad. Sci. USA *111*, 3626–3631.

Buehlmann, A., and Deco, G. (2010). Optimal information transfer in the cortex through synchronization. PLoS Comput. Biol. *6*, 6.

Buffalo, E.A., Fries, P., Landman, R., Liang, H., and Desimone, R. (2010). A backward progression of attentional effects in the ventral stream. Proc. Natl. Acad. Sci. USA *107*, 361–365.

Buffalo, E.A., Fries, P., Landman, R., Buschman, T.J., and Desimone, R. (2011). Laminar differences in gamma and alpha coherence in the ventral stream. Proc. Natl. Acad. Sci. USA *108*, 11262–11267.

Buzsáki, G., and Wang, X.J. (2012). Mechanisms of gamma oscillations. Annu. Rev. Neurosci. *35*, 203–225.

Cardin, J.A., Carlén, M., Meletis, K., Knoblich, U., Zhang, F., Deisseroth, K., Tsai, L.H., and Moore, C.I. (2009). Driving fast-spiking cells induces gamma rhythm and controls sensory responses. Nature *459*, 663–667.

Chen, L.L., Madhavan, R., Rapoport, B.I., and Anderson, W.S. (2013). Real-time brain oscillation detection and phase-locked stimulation using autoregressive spectral estimation and time-series forward prediction. IEEE Trans. Biomed. Eng. *60*, 753–762.

Fries, P. (2005). A mechanism for cognitive dynamics: neuronal communication through neuronal coherence. Trends Cogn. Sci. *9*, 474–480.

Fries, P. (2015). Rhythms for cognition: communication through coherence. Neuron *88*, 220–235.

Fries, P., Reynolds, J.H., Rorie, A.E., and Desimone, R. (2001). Modulation of oscillatory neuronal synchronization by selective visual attention. Science *291*, 1560–1563.

Fries, P., Womelsdorf, T., Oostenveld, R., and Desimone, R. (2008). The effects of visual stimulation and selective visual attention on rhythmic neuronal synchronization in macaque area V4. J. Neurosci. *28*, 4823–4835.

Grothe, I., Neitzel, S.D., Mandon, S., and Kreiter, A.K. (2012). Switching neuronal inputs by differential modulations of gamma-band phase-coherence. J. Neurosci. *32*, 16172–16180.

Haider, B., Schulz, D.P., Häusser, M., and Carandini, M. (2016). Millisecond coupling of local field potentials to synaptic currents in the awake visual cortex. Neuron *90*, 35–42.

Jia, X., Tanabe, S., and Kohn, A. (2013). γ and the coordination of spiking activity in early visual cortex. Neuron *77*, 762–774.

Liang, H., Bressler, S.L., Buffalo, E.A., Desimone, R., and Fries, P. (2005). Empirical mode decomposition of field potentials from macaque V4 in visual spatial attention. Biol. Cybern. *92*, 380–392.

Lowet, E., Roberts, M.J., Bosman, C.A., Fries, P., and De Weerd, P. (2016). Areas V1 and V2 show microsaccade-related 3-4-Hz covariation in gamma power and frequency. Eur. J. Neurosci. *43*, 1286–1296.

Lu, Y., Truccolo, W., Wagner, F.B., Vargas-Irwin, C.E., Ozden, I., Zimmermann, J.B., May, T., Agha, N.S., Wang, J., and Nurmikko, A.V. (2015). Optogenetically induced spatiotemporal gamma oscillations and neuronal spiking activity in primate motor cortex. J. Neurophysiol. *113*, 3574–3587.

Maris, E., Womelsdorf, T., Desimone, R., and Fries, P. (2013). Rhythmic neuronal synchronization in visual cortex entails spatial phase relation diversity that is modulated by stimulation and attention. Neuroimage *74*, 99–116.

Michalareas, G., Vezoli, J., van Pelt, S., Schoffelen, J.M., Kennedy, H., and Fries, P. (2016). Alpha-beta and gamma rhythms subserve feedback and feedforward influences among human visual cortical areas. Neuron *89*, 384–397.

Nichols, T.E., and Holmes, A.P. (2002). Nonparametric permutation tests for functional neuroimaging: a primer with examples. Hum. Brain Mapp. *15*, 1–25.

Oostenveld, R., Fries, P., Maris, E., and Schoffelen, J.M. (2011). FieldTrip: Open source software for advanced analysis of MEG, EEG, and invasive electrophysiological data. Comput. Intell. Neurosci. *2011*, 156869.

Payne, B.R. (1993). Evidence for visual cortical area homologs in cat and macaque monkey. Cereb. Cortex *3*, 1–25.

Ray, S., and Maunsell, J.H. (2015). Do gamma oscillations play a role in cerebral cortex? Trends Cogn. Sci. *19*, 78–85.

Reynolds, J.H., Chelazzi, L., and Desimone, R. (1999). Competitive mechanisms subserve attention in macaque areas V2 and V4. J. Neurosci. *19*, 1736–1753.

Roberts, M.J., Lowet, E., Brunet, N.M., Ter Wal, M., Tiesinga, P., Fries, P., and De Weerd, P. (2013). Robust gamma coherence between macaque V1 and V2 by dynamic frequency matching. Neuron *78*, 523–536.

Salinas, E., and Sejnowski, T.J. (2001). Correlated neuronal activity and the flow of neural information. Nat. Rev. Neurosci. *2*, 539–550.

Salkoff, D.B., Zagha, E., Yüzgeç, Ö., and McCormick, D.A. (2015). Synaptic mechanisms of tight spike synchrony at gamma frequency in cerebral cortex. J. Neurosci. *35*, 10236–10251.

Siegle, J.H., Pritchett, D.L., and Moore, C.I. (2014). Gamma-range synchronization of fast-spiking interneurons can enhance detection of tactile stimuli. Nat. Neurosci. *17*, 1371–1379.

Tiesinga, P., and Sejnowski, T.J. (2009). Cortical enlightenment: are attentional gamma oscillations driven by ING or PING? Neuron *63*, 727–732.

van Elswijk, G., Maij, F., Schoffelen, J.M., Overeem, S., Stegeman, D.F., and Fries, P. (2010). Corticospinal beta-band synchronization entails rhythmic gain modulation. J. Neurosci. *30*, 14332–14341.

van Kerkoerle, T., Self, M.W., Dagnino, B., Gariel-Mathis, M.A., Poort, J., van der Togt, C., and Roelfsema, P.R. (2014). Alpha and gamma oscillations characterize feedback and feedforward processing in monkey visual cortex. Proc. Natl. Acad. Sci. USA. *111*, 4481–4488.

Vinck, M., van Wingerden, M., Womelsdorf, T., Fries, P., and Pennartz, C.M. (2010). The pairwise phase consistency: a bias-free measure of rhythmic neuronal synchronization. Neuroimage *51*, 112–122.

Vinck, M., Battaglia, F.P., Womelsdorf, T., and Pennartz, C. (2012). Improved measures of phase-coupling between spikes and the local field potential. J. Comput. Neurosci. *33*, 53–75.

Vinck, M., Womelsdorf, T., Buffalo, E.A., Desimone, R., and Fries, P. (2013). Attentional modulation of cell-class-specific gamma-band synchronization in awake monkey area V4. Neuron *80*, 1077–1089.

Whittington, M.A., Traub, R.D., Kopell, N., Ermentrout, B., and Buhl, E.H. (2000). Inhibition-based rhythms: experimental and mathematical observations on network dynamics. Int. J. Psychophysiol. *38*, 315–336.

Womelsdorf, T., Fries, P., Mitra, P.P., and Desimone, R. (2006). Gamma-band synchronization in visual cortex predicts speed of change detection. Nature *439*, 733–736.

Womelsdorf, T., Schoffelen, J.M., Oostenveld, R., Singer, W., Desimone, R., Engel, A.K., and Fries, P. (2007). Modulation of neuronal interactions through neuronal synchronization. Science *316*, 1609–1612.

Zandvakili, A., and Kohn, A. (2015). Coordinated neuronal activity enhances corticocortical communication. Neuron *87*, 827–839.